Applied Physics Letters ARTICLE scitation.org/journal/apl

Observation of unidirectional spin Hall magnetoresistance in amorphous $PtSn_4$/CoFeB bilayers

Cite as: Appl. Phys. Lett. **121**, 092401 (2022); doi: 10.1063/5.0097355
Submitted: 28 April 2022 · Accepted: 5 August 2022 ·
Published Online: 29 August 2022

Yihong Fan,[1] Zach Cresswell,[2] Silu Guo,[2] Delin Zhang,[1] Thomas J. Peterson,[3] Jinming Liu,[1] Yang Lv,[1] K. Andre Mkhoyan,[2] and Jian-Ping Wang[1,a)]

AFFILIATIONS

[1]Department of Electrical and Computer Engineering, University of Minnesota, 200 Union St. SE, Minneapolis, Minnesota 55455, USA
[2]Department of Chemical Engineering and Materials Science, University of Minnesota, 421 Washington Ave. SE, Minneapolis, Minnesota 55455, USA
[3]School of Physics and Astronomy, University of Minnesota, 116 Church St. SE, Minneapolis, Minnesota 55455, USA

[a)]Author to whom correspondence should be addressed: jpwang@umn.edu

ABSTRACT

Unidirectional spin Hall magnetoresistance (USMR) is a magnetoresistance effect with potential applications to read two-terminal spin–orbit-torque (SOT) devices directly. In this work, we observed a large USMR value (up to 0.7×10^{-11} per A/cm^2, 50% larger than reported values from heavy metals) in sputtered amorphous $PtSn_4$/CoFeB bilayers. Ta/CoFeB bilayers with interfacial MgO insertion layers are deposited as control samples. The control experiments show that increasing the interfacial resistance can increase the USMR value, which is the case in $PtSn_4$/CoFeB bilayers. The observation of a large USMR value in an amorphous spin–orbit-torque material has provided an alternative pathway for USMR application in two-terminal SOT devices.

As emerging beyond-CMOS technologies, spin–orbit torque (SOT)-based memory and logic devices[1–6] can be improved in two aspects. First, with the device scaling down to advanced node size, the device geometry is at the same magnitude as the polycrystalline grain size, where the existence of domain wall pinning effects[7,8] at crystal boundaries cannot be negligible. Thus, film uniformity is of vital importance for device consistency. Second, requiring a magnetic tunnel junction (MTJ)[9,10] or a Hall bar structure[11–13] for reading, a unit SOT device has a relatively complex structure for fabrication.[14]

Compared to polycrystalline materials, amorphous materials have more uniform microstructures even at the nanoscale, which is good to eliminate performance variations between devices.[15,16] Crystalline $PtSn_4$ was reported as a Dirac semimetal.[4] Semimetals were proposed to have a smaller energy consumption due to their small resistivity and large charge to spin conversion efficiency, which originates from their strong spin–orbit coupling at bulk Dirac nodes.[17–20] In our previous work, we have shown that amorphous $PtSn_4$ films sputtered by using a $PtSn_4$ compound target can produce a relatively large charge to spin conversion efficiency (~0.35)[21] with relatively small resistivity (~305 $\mu\Omega$ cm), compared to other topological materials.

To effectively read SOT switching, unidirectional spin Hall magnetoresistance (USMR) was proposed as a prospective candidate.[22–28] Originating from the interfacial spin accumulation, which induces an effective magnetic layer, USMR in metallic systems is similar to current-in-plane giant magnetoresistance (CIP-GMR), which has a longitudinal magnetoresistance when the magnetization is switched by 180°. Thus, a simple two-terminal SOT device is possible if USMR is used for reading.[27] Previous USMR research has mostly focused on crystalline and/or polycrystalline bilayers, USMR in amorphous systems is not reported yet. The CIP-GMR model has pointed out that an interfacial spin accumulation may play an important role in obtaining a large USMR value.[22,24] Compared to polycrystalline materials, amorphous materials are supposed to have a larger interfacial resistance due to their disordered structure, which may lead to a larger interfacial spin accumulation at the ferromagnetic (FM)/spin Hall material interface[29] and, thus, a larger USMR value.

In this work, we report a large USMR value up to 0.7×10^{-11} per current density (A/cm^2) in amorphous $PtSn_4$/CoFeB bilayers. This value is 50% larger than reported values in crystalline heavy metal systems.[22,23] We designed control experiments to adjust the interfacial

resistance. The control samples have shown that increasing interfacial resistance can result in larger interfacial spin accumulation, which led to a larger USMR value compared to a transparent interface.

We deposited a $PtSn_4$(5)/CoFeB(2.5, 5, 7.5, 10)/MgO(2)/Ta(2) multilayer structure, where the parenthesis denotes thickness in nanometers, by magnetron sputtering onto a thermally oxidized Si/SiO2 substrate. $PtSn_4$ was first grown on the substrate with a base pressure of 8×10^{-8} Torr and an Ar working pressure of 4.5 mTorr and then transferred to another sputtering chamber for CoFeB deposition. A 30-s *in situ* etching was performed to remove the potential oxidization during the transfer. A CoFeB(2.5, 5, 7.5, 10)/MgO(2)/Ta(2) layer stack was then grown under 8×10^{-8} Torr base pressure and 1.5 mTorr Ar working pressure.

An additional $PtSn_4$(20)/MgO(2)/Ta(2) film was also deposited under the same condition for scanning transmission electron microscopy (STEM) study (see Methods paragraph for details). Figure 1(a) shows a bright-field conventional TEM (CTEM) image of the layer stack. The $PtSn_4$ layer appears to be amorphous since no crystalline features are observed in these high-resolution CTEM images. In contrast, crystalline grains are visible in the adjacent MgO layer, indicating that the MgO layer is polycrystalline [Fig. 1(a)]. The $PtSn_4$ film shows relatively high uniformity. Additional elemental analysis of the layers using energy dispersive x-ray (EDX) spectroscopy was also performed, and the results are shown in Fig. 1(b). The measured Sn to Pt atomic ratio is 3.71, which is close to the expected composition of $PtSn_4$. The difference in atomic mass and vapor pressure between Sn and Pt may be the reason for this slight composition shift.

We then characterized the charge to spin conversion efficiency for the $PtSn_4$ samples via spin-torque ferromagnetic resonance (ST-FMR). The $PtSn_4$(5)/CoFeB(x)/MgO(2)/Ta(2) samples ($x = 2.5$, 5, 7.5, and 10) were first patterned into microstrips 40 μm in width and 60 μm in length. The electrode for the ST-FMR measurements was then deposited onto the microstrip, as shown in Fig. 2(a). The patterned devices were then connected to the GHz generator and nanovoltmeter as shown in Fig. 2(a) with a capacitor and an inductor to block the DC and RF current components, respectively, to carry out the ST-FMR measurements.[2,30,31] The ST-FMR signal of the $PtSn_4$(5)/CoFeB(5)/MgO(2)/Ta(2) sample under 9 GHz is shown in Fig. 2(b), which can be separated into symmetric and antisymmetric Lorentzian parts.[32,33] A well-established analysis method[30] gives the charge to spin conversion ratio by the following equation:

$$\frac{\tau_{Oe} + \tau_{FL}}{\tau_{AD}} = \left(\frac{J_S}{J_C}\right)^{-1} \frac{e\mu_0 M_S}{\hbar} t_{CFB} d_{PtSn} + \frac{\tau_{FL}}{\tau_{AD}}, \quad (1)$$

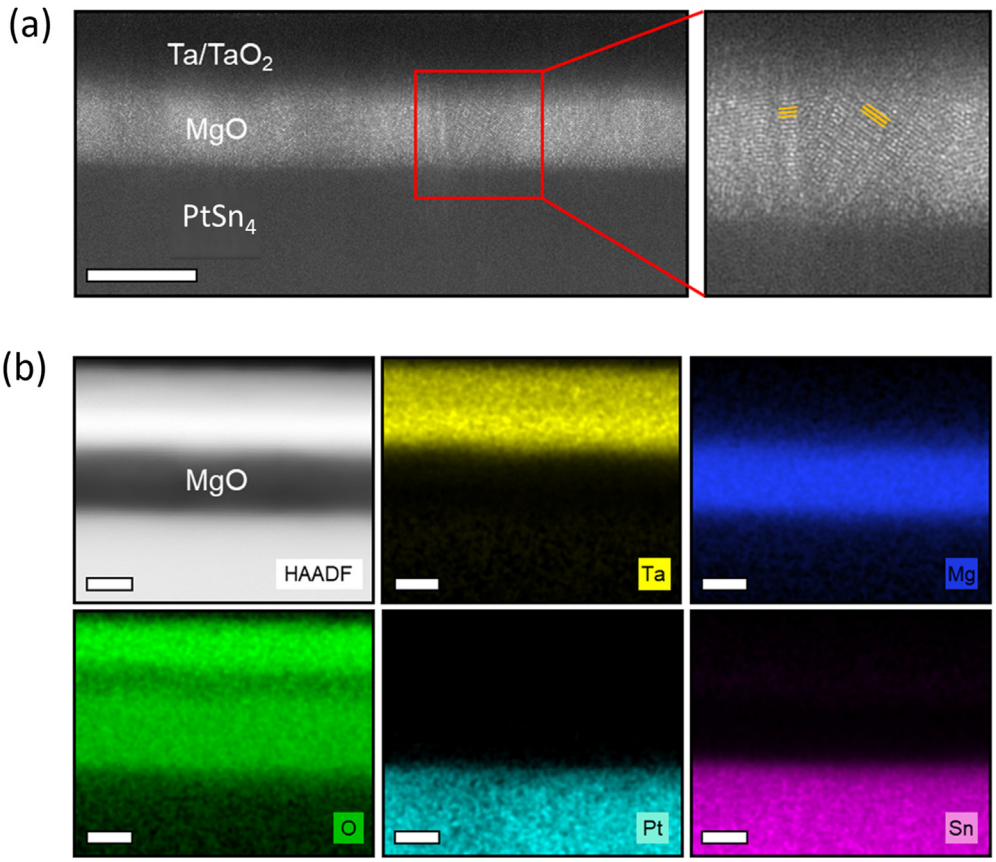

FIG. 1. Electron microscopy analysis of the device. (a) Conventional TEM image of the device showing functional Ta/TaO_2, MgO, and Pt_xSn_y layers. The MgO layer is polycrystalline. The lattice fringes in two neighboring grains, indicated by the yellow lines, are visible in the magnified region of MgO highlighted by red square and (b) HAADF-STEM image and complementary EDX elemental maps of the layer stack of the device. The scale bar is 5 nm.

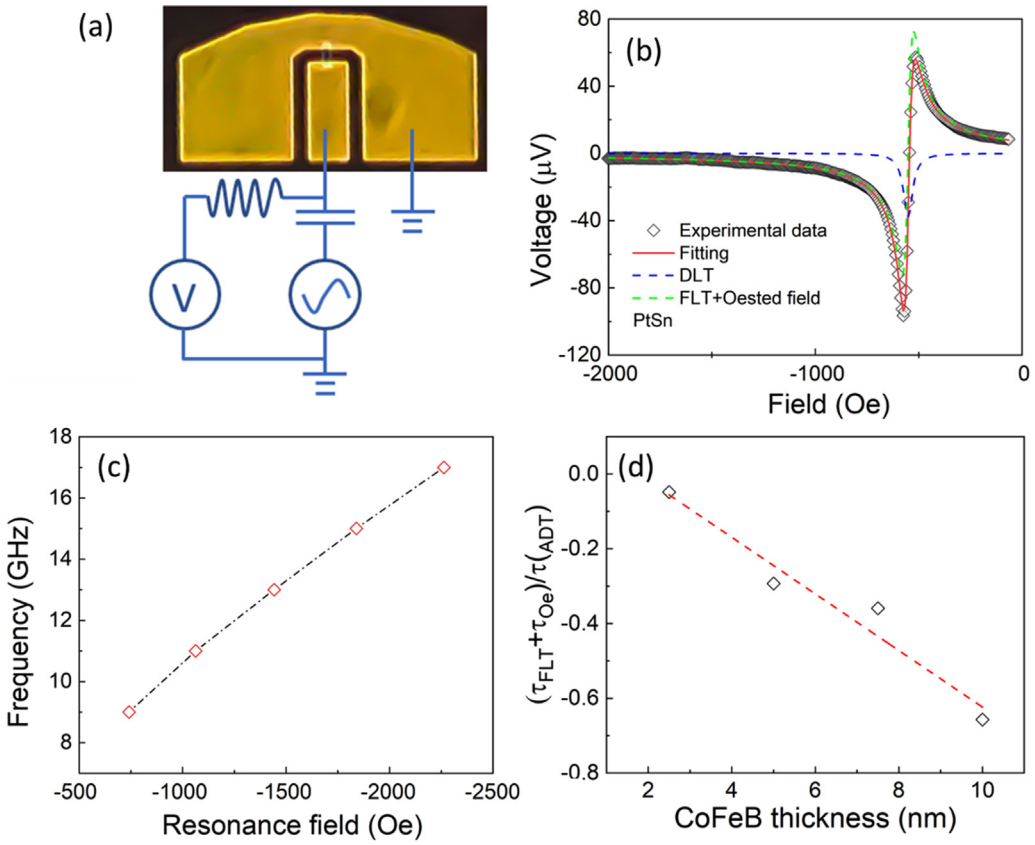

FIG. 2. (a) Optical image of the waveguide structure for the ST-FMR measurement. An illustration of the measurement setup is also shown. (b) The experimental data and fitting results for sample $PtSn_4$(5 nm)/CoFeB(5 nm)/capping, where the black squares are the experimental data, the red line is the fitting result, and the blue (green) dashed line is the symmetric (antisymmetric) Lorentzian, which stands for the DLT (FLT and Oersted field) component. (c) Kittel fitting of the $PtSn_4$(5 nm)/CoFeB(5 nm)/capping sample, which is used to obtain the effective magnetization. (d) $\frac{\tau_{Oe}+\tau_{FL}}{\tau_{AD}}$ vs CoFeB thickness fitting. The slope is used to calculate the charge to spin conversion ratio.

where τ_{Oe} (τ_{FL}, τ_{AD}) is the Oersted field torque [field like torque (FLT), damping like torque (DLT)], M_S is the CoFeB saturation magnetization, and t_{CFB} (d_{PtSn}) is the thickness of CoFeB ($PtSn_4$) layers. We can obtain the ratio $\frac{\tau_{Oe}+\tau_{FL}}{\tau_{AD}}$ by the symmetric and antisymmetric Lorentzian voltage: $\frac{\tau_{Oe}+\tau_{FL}}{\tau_{AD}} = \frac{V_{Asym}}{V_{Sym}}\left[1+(4\pi M_{eff}/H_0)\right]^{-\frac{1}{2}}$, where M_{eff} is the effective magnetization of the CoFeB layer, which can be obtained by the Kittel formula $f = \frac{\gamma}{2\pi}\sqrt{H_0(H_0+4\pi M_{eff})}$, as shown in Fig. 2(c). The linear dependence fitting of $\frac{\tau_{Oe}+\tau_{FL}}{\tau_{AD}}$ and t_{CFB} is shown in Fig. 2(d), where we can extract the charge to spin conversion ratio $\frac{J_S}{J_C}$ in Eq. (1), which is 0.32 ± 0.09 for the amorphous $PtSn_4$ layer. The results show that amorphous $PtSn_4$ has a charge to spin conversion ratio comparable to heavy metals,[2,10,16] which is favored to obtain a large USMR value.[22–24]

The film stack was then patterned into a Hall bar structure 10 μm in width and 60 μm in length as shown in Fig. 3(a). The distance between the two Hall channels is 35 μm from center to center (30 μm between the edges). The current flows in the x-direction, and the longitudinal voltage was measured between the Hall channels in the same direction. We applied an AC with an amplitude of 1.2 mA and a frequency of 133 Hz to the sample and measured the second harmonic voltage between the longitudinal Hall channels by an SR830 lock-in amplifier, as shown in Fig. 3(a). A 5 T magnetic field was applied in the XY plane, and the angle θ between the external magnetic field and the current was rotated in-plane. The resulting angular dependence of the second harmonic signal is shown in Fig. 3(b) (black curve), where the peak-to-peak voltage is 18 μV. (The constant measurement background is removed to show the signal scales better.)

The second harmonic signals may have three origins: USMR, thermal effects [anomalous Nernst effect (ANE) and spin Seebeck effect (SSE)], and SOT contributions. To obtain the USMR signals, each contribution needs to be separated. Here, we measured the angular dependence of the transverse second harmonic signal under different fields, as shown in Fig. 3(c). The field dependence of the SOT and thermal contribution is

$$V_{SOT+thermal} = -\frac{1}{2}R_{AHE}\frac{H_{DL}}{H_{ext}+H_k} + R_{PHE}\frac{H_{FL}}{H_{ext}} + I\,\alpha\,\nabla T, \quad (2)$$

where H_{DL} (H_{FL}) is the damping like (field like) torque effective field, H_{ext} is the external field, H_k is the anisotropy field, R_{AHE} (R_{PHE}) is the anomalous Hall effect (planar Hall effect) resistance, I is the current, α is a constant, and ∇T is the temperature gradient. We plotted the

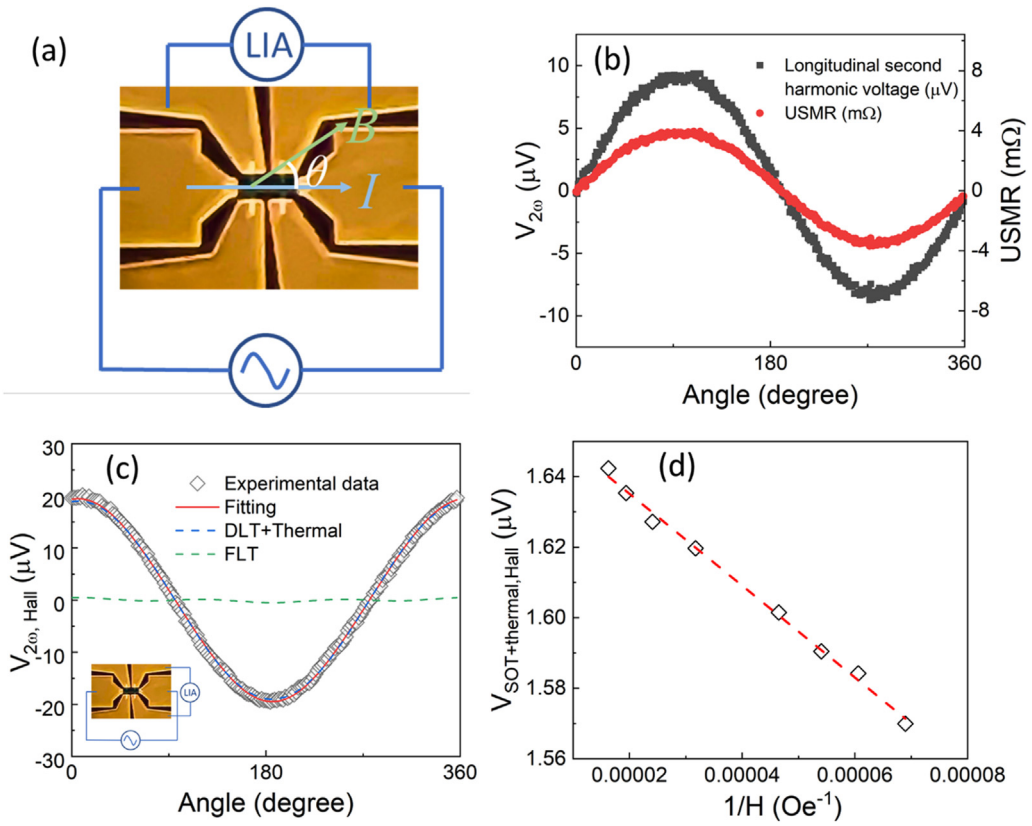

FIG. 3. (a) Optical image of the Hall bar structure for the sample $PtSn_4$(5 nm)/CoFeB(7.5 nm)/capping and the illustration of the AC measurement. (b) The longitudinal second harmonic angular dependent voltage (black line) and the resulting USMR (red line) under a 5 T magnetic field. The left axis is the voltage, and the right axis is the resistance change. (c) Transverse second harmonic measurement for the same device. The curve is fitted to remove the FLT contribution and get the DLT and thermal effect contribution. The blue (green) dashed line stands for the DLT plus the thermal part (the FLT part). The measurement setup is shown in the inside part. (d) Field dependence of the DLT and thermal contribution, where the interception is the thermal contribution in the transverse direction.

transverse voltage against $1/(H_{ext} + H_k)$, as shown in Fig. 3(d). At 5 T, the SOT contribution is quite small compared to the intercept, which represents the ANE and SSE contributions. Thus, the SOT contribution is negligible at high magnetic fields.

A scaling method is used to calculate the ANE and SSE contributions in the longitudinal direction.[22] The ANE and SSE voltages are proportional to the length of the area that is measured as a result of a perpendicular temperature gradient. The thermal contribution for the longitudinal direction can be estimated by the geometry factors

$$R_{thermal,\,longitudinal} = \frac{l}{w} R_{thermal,\,Hall}, \tag{3}$$

where l is the length between the two Hall channels (30 μm from edge to edge) and w is the width of the Hall bar (10 μm). The scaled thermal contribution is ~50% of the total signal, as shown in Fig. 3(b).

With the estimated thermal contribution, the final USMR value is extracted and shown in Fig. 3(b) (red curve). Considering the USMR is a nonlinear magnetoresistance and is proportional to the current, we calculated the USMR ratio per unit current density (the current density is 0.7×10^6 A/cm^2, and the sample resistance is 870 Ω), giving 0.7×10^{-11} per unit current density (A/cm^2). The USMR value reported in amorphous $PtSn_4$ is 50% larger than reported values in heavy metals.[22–24]

The CIP-GMR is dependent on the relative magnetization of the two magnetic layers.[34,35] In the case of USMR, one of the magnetic layers is an effective magnetic layer, which is a layer with spin-polarized electrons accumulated at the interface. Both field-dependent measurement and current dependent measurement show the majority of the USMR signal is in the spin-dependent regime, in which the CIP-GMR is the major contribution to the USMR signal[23] (see the supplementary material for details). Compared to heavy metal/ferromagnetic metal bilayers, amorphous $PtSn_4$ has a relatively large resistivity (~305 $\mu\Omega$cm) and a more disordered structure at the interface with the ferromagnetic layer. Based on the resistivity values of $PtSn_4$ and CoFeB, the calculated resistance for the USMR device should be ~809 Ω, which is smaller than the real device resistance (~870 Ω) even with the contribution of the capping Ta layer that may not be fully oxidized (see the supplementary material for error analysis). This result suggests a larger interfacial resistance. Though limited by accuracy, direct detection of interfacial spin accumulation has shown the upper limit of the spin accumulation decreases with top material resistivity (and interfacial resistance as well) in Pt/normal metal bilayers.[36]

A larger interfacial resistivity usually means more interfacial defects, which may trap the electrons and result in more spin-polarized electron accumulation at the interface. As a result, the effective magnetization of the accumulated spin-polarized electrons also increases as the interfacial resistance increases. This leads to a larger effective magnetization at the interface and a larger USMR ratio in amorphous material/ferromagnetic bilayers.

To verify this explanation, we fabricated two well-studied multilayer stacks as control samples: Ta(5)/(MgO(0.3))/CoFeB(5)/MgO(2)/Ta(1.5) and Ta(2)/(MgO(0.3))/Pt(4)/Co(5)/MgO(2)/Ta(1.5) (thickness in nm). A 0.3 nm MgO layer was inserted in one sample for both structures between the heavy metal layer and the magnetic layer. If the previous explanation is to hold, this will increase the interfacial resistance and, thus, enhance the accumulation of the spin-polarized electrons, as shown in Fig. 4(a). Since the CoFeB layer has a large dead layer (~0.8 nm, referring to the supplementary material for detailed information), inserting MgO will not significantly change its magnetization and interfacial spin scattering. Previous studies have reported a range of the dead layer thickness in Ta/CFB bilayers from ~0.3 to ~0.85 nm, depending on the fabrication condition and diffusions.[37,38] A large dead layer value is not rare at the Ta/CFB interface. However, adding a MgO layer to the Pt/Co interface will oxidize the interfacial Co layer and, thus, change the magnetization and interfacial scattering process.[39,40] The measured second harmonic voltage in the Ta(2 nm)/Pt(4 nm)/Co(5 nm) sample is illustrated in Fig. 4(b). With a relative large contribution of the field-like torque, Fig. 4(b) is plotted with a 90° phase difference compared to Fig. 3(b) for a clearer view. We measured the USMR and processed the data with the same analyzing method. The results are shown in Table I. With a MgO insertion layer,

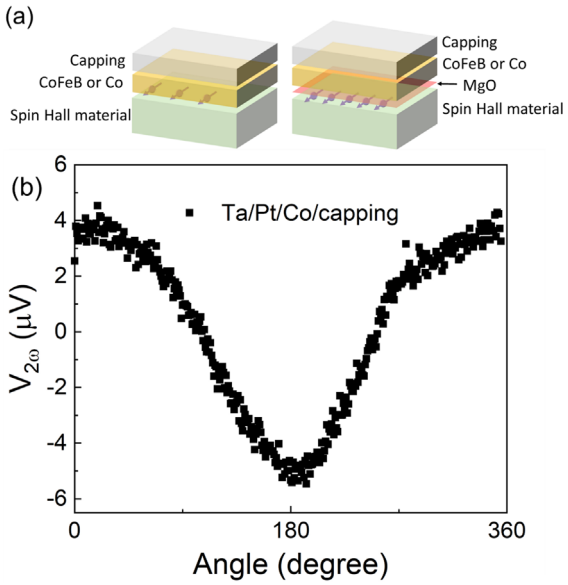

FIG. 4. (a) Illustration of the control sample. The magnetic layer is CoFeB or Co with a MgO layer inserted at the interface. The insertion MgO layer can change the spin accumulation at the interface. (b) Second harmonic signal of the Ta(2 nm)/Pt(4 nm)/Co(5 nm)/capping control sample. The figure is plotted with a 90° phase difference compared to Fig. 3(b) for a clearer view.

TABLE I. The USMR ratio per unit current density for different control sample structures. These results suggest that increasing interfacial resistance can lead to an increase in the USMR value, which can explain the relatively large USMR value in $PtSn_4$/CoFeB bilayers.

Structure (layer thickness in nm)	USMR ratio per current density (A/cm^2)
Ta(5)/CFB(5)/capping	4.3×10^{-13}
Ta(5)/MgO(0.3)/CFB(5)/capping	4.6×10^{-13}
Ta(2)/Pt(4)/Co(5)/capping	3.2×10^{-13}
Ta(2)/Pt(4)/MgO(0.3)/Co(5)/capping	1.0×10^{-13}

the CoFeB control samples show similar or larger USMR values due to the increase in the interfacial spin accumulation without changing the interfacial magnetization. Even if this system may get larger SOT efficiency compared to the case without MgO insertion,[40,41] the Co control sample shows a smaller USMR value due to the oxidization of the Co layer leading to a smaller reference layer magnetization as well as a smaller interfacial spin scattering, since the Co/Pt interface does not have a large dead layer.[42] These results imply that increasing interfacial resistance without reducing the interfacial magnetization can increase the USMR value in an optimized system.

In summary, we deposited amorphous SOT $PtSn_4$/CoFeB bilayers by magnetron sputtering. TEM and AFM images show uniform amorphous microstructure across the whole film area. ST-FMR was used to determine a charge-to-spin conversion ratio of ~0.32 in this bilayer structure. This relatively large charge-to-spin conversion ratio is beneficial to achieving a large USMR value. USMR up to 0.7×10^{-11} per unit current density (A/cm^2) was demonstrated in $PtSn_4$/CoFeB bilayers, which is 50% larger than that of any reported crystalline heavy metal SOT materials. Based on the current-in-plane GMR model, the large USMR value possibly originates from increased interfacial spin accumulation. The amorphous nature of $PtSn_4$ leads to a larger interfacial resistance, and thus, amorphous structures may be favored to obtain a larger USMR. This was verified by the control samples Ta/Pt/CoFeB and Ta/Pt/Co with a MgO insertion layer at the FM/HM interface, which showed that increasing the interfacial resistance without reducing the magnetization can increase the USMR value. The enhanced USMR value in amorphous materials, as well as the underlying physics, has shown potential for amorphous SOT materials in USMR-related applications.

The details of the sample growth and characterization are shown below.

The $PtSn_4$ layer is grown by an eight-target sputtering system with *in situ* heaters. The CoFeB has a composition $Co_{20}Fe_{60}B_{20}$ and is grown by a Shamrock sputtering system (see https://nanospin.umn.edu/sputtering-systems for facility info). The CoFeB and capping Ta layer is grown at 100 W with an Advanced Energy MDX 1.5 K power supply, while the capping MgO layer is grown at 320 W using an Advanced Energy RFX600 power supply.

The GHz signal in ST-FMR measurement is generated by an Agilent E8241A RF power generator. The DC signal is measured by a Keithley 2182A nanovoltmeter. The external in-plane magnetic field is rotated at 45° to maximize the ST-FMR signal.

The details of TEM characterization are shown as follows. First, a 50 nm am-C layer was deposited onto the surface of the device using a

sputter coater. Then, a 30–50 nm thick cross-sectional lamella was prepared through a focused ion beam (FIB) (FEI Helios NanoLab G4 dual-beam focused ion beam). Before FIB-cutting, additional layers and the am-C protection and Pt were deposited on the region of interest. ThermoFisher Scientific Talos F200X G2 S-TEM with Super-X EDX spectrometer was used to obtain conventional TEM, high-angle annular dark-field (HAADF) - scanning transmission electron microscopy (STEM) images, and STEM-EDX maps. The STEM was operated at an accelerating voltage of 200 kV. The probe convergence angle was 10.5 mrad for HAADF-STEM imaging. For STEM-EDX-mapping, the beam current ranged from 300 to 400 pA.

See the supplementary material for the determination of the source of USMR, the detail of the CoFeB dead layer thickness, and the resistance analysis.

This work was supported, in part, by SMART, one of the seven centers of nCORE, a Semiconductor Research Corporation Program, sponsored by the National Institute of Standards and Technology (NIST) and by the University of Minnesota (UMN) Materials Research Science and Engineering Center (MRSEC) Program under Award No. DMR-2011401. This work utilized the College of Science and Engineering (CSE) Characterization Facility at the University of Minnesota (UMN) supported, in part, by the National Science Foundation (NSF) through the UMN Material Research Science and Engineering Center (MRSEC) Program. Portions of this work were conducted in the Minnesota Nano Center, which is supported by the National Science Foundation through the National Nano Coordinated Infrastructure Network (NNCI) under Award No. ECCS-2025124. D.Z. and T.J.P. are partially supported by ASCENT, one of six centers of JUMP, a Semiconductor Research Corporation program that is sponsored by MARCO and Defense Advanced Research Projects Agency (DARPA). J.T.H. acknowledges support from a Doctoral Dissertation Fellowship received from the graduate school at the University of Minnesota. J.-P.W. also acknowledges support from the Robert Hartmann Endowed Chair Professorship.

AUTHOR DECLARATIONS

Conflict of Interest

The authors have no conflicts to disclose.

Author Contributions

Yihong Fan: Conceptualization (equal); Data curation (equal); Formal analysis (equal); Investigation (equal); Methodology (equal); Writing – original draft (equal); Writing – review and editing (equal). **Zach Cresswell:** Conceptualization (equal); Formal analysis (equal); Investigation (equal); Writing – review and editing (equal). **Silu Guo:** Conceptualization (equal); Data curation (equal); Formal analysis (lead); Writing – original draft (supporting). **Delin Zhang:** Conceptualization (equal); Writing – review and editing (equal). **Thomas J. Peterson:** Conceptualization (equal); Methodology (equal); Writing – review and editing (equal). **Jinming Liu:** Conceptualization (equal); Data curation (equal); Writing – review and editing (equal). **Yang Lv:** Investigation (equal); Supervision (equal); Writing – review and editing (equal). **K. Andre Mkhoyan:** Formal analysis (equal); Funding acquisition (equal); Supervision (equal); Writing – original draft (equal). **Jian-Ping Wang:** Conceptualization (equal); Funding acquisition (equal); Project administration (equal); Supervision (equal); Writing – review and editing (equal).

DATA AVAILABILITY

The data that support the findings of this study are available from the corresponding author upon reasonable request.

REFERENCES

[1]I. M. Miron, G. Gaudin, S. Auffret *et al.*, "Current-driven spin torque induced by the Rashba effect in a ferromagnetic metal layer," Nat. Mater. **9**(3), 230–234 (2010).
[2]L. Liu, T. Moriyama, D. C. Ralph *et al.*, "Spin-torque ferromagnetic resonance induced by the spin Hall effect," Phys. Rev. Lett. **106**(3), 036601 (2011).
[3]X. Fan, H. Celik, J. Wu *et al.*, "Quantifying interface and bulk contributions to spin–orbit torque in magnetic bilayers," Nat. Commun. **5**(1), 3042 (2014).
[4]J. Ding, C. Liu, V. Kalappattil *et al.*, "Switching of a magnet by spin–orbit torque from a topological Dirac semimetal," Adv. Mater. **33**(23), 2005909 (2021).
[5]K. Tang, Z. Wen, Y.-C. Lau *et al.*, "Magnetization switching induced by spin–orbit torque from Co_2MnGa magnetic Weyl semimetal thin films," Appl. Phys. Lett. **118**(6), 062402 (2021).
[6]Q. Shao, P. Li, L. Liu *et al.*, "Roadmap of spin-orbit torques," IEEE Trans. Magn. **57**, 1–39 (2021).
[7]S. Zhang, S. Luo, N. Xu *et al.*, "A spin–orbit-torque memristive device," Adv. Electron. Mater. **5**(4), 1800782 (2019).
[8]J. M. Lee, K. Cai, G. Yang *et al.*, "Field-free spin–orbit torque switching from geometrical domain-wall pinning," Nano Lett. **18**(8), 4669–4674 (2018).
[9]L. Liu, O. J. Lee, T. J. Gudmundsen *et al.*, "Current-induced switching of perpendicularly magnetized magnetic layers using spin torque from the spin Hall effect," Phys. Rev. Lett. **109**(9), 096602 (2012).
[10]L. Liu, C.-F. Pai, Y. Li *et al.*, "Spin-torque switching with the giant spin Hall effect of tantalum," Science **336**(6081), 555–558 (2012).
[11]C. O. Avci, A. Quindeau, C.-F. Pai *et al.*, "Current-induced switching in a magnetic insulator," Nat. Mater. **16**(3), 309–314 (2017).
[12]Y.-C. Lau, D. Betto, K. Rode *et al.*, "Spin–orbit torque switching without an external field using interlayer exchange coupling," Nat. Nanotechnol. **11**(9), 758–762 (2016).
[13]Y. Fan, P. Upadhyaya, X. Kou *et al.*, "Magnetization switching through giant spin–orbit torque in a magnetically doped topological insulator heterostructure," Nat. Mater. **13**(7), 699–704 (2014).
[14]J.-P. Wang, S. S. Sapatnekar, C. H. Kim *et al.*, "A pathway to enable exponential scaling for the beyond-CMOS era," in Proceedings of the 54th Annual Design Automation Conference 2017, 2017.
[15]C.-H. Hsu, J. Karel, N. Roschewsky *et al.*, "Spin-orbit torque generated by amorphous FeSi," e-print arXiv:2006.07786 (2020).
[16]T.-C. Wang, T.-Y. Chen, C.-T. Wu *et al.*, "Comparative study on spin–orbit torque efficiencies from W/ferromagnetic and W/ferrimagnetic heterostructures," Phys. Rev. Mater. **2**(1), 014403 (2018).
[17]Y. Wu, L.-L. Wang, E. Mun *et al.*, "Dirac node arcs in $PtSn_4$," Nat. Phys. **12**(7), 667–671 (2016).
[18]J. Yan, X. Luo, J. J. Gao *et al.*, "The giant planar Hall effect and anisotropic magnetoresistance in Dirac node arcs semimetal $PtSn_4$," J. Phys.: Condens. Matter **32**(31), 315702 (2020).
[19]A. Bose, J. N. Nelson, X. S. Zhang *et al.*, "Effects of anisotropic strain on spin–orbit torque produced by the Dirac nodal line semimetal IrO_2," ACS Appl. Mater. Interfaces **12**(49), 55411–55416 (2020).
[20]T. Misawa and K. Nomura, "Semi-quantized spin pumping and spin-orbit torques in topological Dirac semimetals," Sci. Rep. **9**(1), 19659 (2019).
[21]J. Liu, Y. Fan, D. Zhang *et al.*, "Element doping enhanced charge-to-spin conversion efficiency in amorphous $PtSn_4$ Dirac semimetal," arXiv:2202.01384 (2022).
[22]C. O. Avci, K. Garello, A. Ghosh *et al.*, "Unidirectional spin Hall magnetoresistance in ferromagnet/normal metal bilayers," Nat. Phys. **11**(7), 570–575 (2015).

[23]C. O. Avci, G. Kevin, A. Ghosh *et al.*, "Origins of the unidirectional spin Hall magnetoresistance in metallic bilayers," Phys. Rev. Lett. **121**(8), 087207 (2018).
[24]S. S.-L. Zhang and G. Vignale, "Theory of unidirectional spin Hall magnetoresistance in heavy-metal/ferromagnetic-metal bilayers," Phys. Rev. B **94**(14), 140411 (2016).
[25]N. H. Duy Khang and P. N. Hai, "Giant unidirectional spin Hall magnetoresistance in topological insulator–ferromagnetic semiconductor heterostructures," J. Appl. Phys. **126**(23), 233903 (2019).
[26]W. P. Sterk, D. Peerlings, and R. A. Duine, "Magnon contribution to unidirectional spin Hall magnetoresistance in ferromagnetic-insulator/heavy-metal bilayers," Phys. Rev. B **99**(6), 064438 (2019).
[27]Y. Lv, J. Kally, D. Zhang *et al.*, "Unidirectional spin-Hall and Rashba–Edelstein magnetoresistance in topological insulator-ferromagnet layer heterostructures," Nat. Commun. **9**(1), 111 (2018).
[28]Y. Lv, J. Kally, T. Liu *et al.*, "Large unidirectional spin Hall and Rashba–Edelstein magnetoresistance in topological insulator/magnetic insulator heterostructures," Appl. Phys. Rev. **9**(1), 011406 (2022).
[29]S. Takahashi and S. Maekawa, "Spin current, spin accumulation and spin Hall effect," Sci. Technol. Adv. Mater. **9**(1), 014105 (2008).
[30]C.-F. Pai, Y. Ou, L. H. Vilela-Leão *et al.*, "Dependence of the efficiency of spin Hall torque on the transparency of Pt/ferromagnetic layer interfaces," Phys. Rev. B **92**(6), 064426 (2015).
[31]C. He, A. Navabi, Q. Shao *et al.*, "Spin-torque ferromagnetic resonance measurements utilizing spin Hall magnetoresistance in $W/Co_{40}Fe_{40}B_{20}/MgO$ structures," Appl. Phys. Lett. **109**(20), 202404 (2016).
[32]P. E. Tannenwald and M. H. Seavey, Jr., "Ferromagnetic resonance in thin films of permalloy," Phys. Rev. **105**(2), 377 (1957).
[33]J. C. Sankey, Y.-T. Cui, J. Z. Sun *et al.*, "Measurement of the spin-transfer-torque vector in magnetic tunnel junctions," Nat. Phys. **4**(1), 67–71 (2008).
[34]M. Djamal, T. Saragi, and M. Barmawi, "Design and development of magnetic sensors based on giant magnetoresistance (GMR) materials," in *Materials Science Forum* (Trans Tech Publications Ltd, 2006), Vol. 517.
[35]R. R. Katti, "Giant magneto-resistive random-access memories based on current-in-plane devices," in *Ultrathin Magnetic Structures IV* (Springer, Berlin/Heidelberg, 2005), pp. 219–252.
[36]C. Stamm, C. Murer, Y. Acremann, M. Baumgartner *et al.*, "X-ray spectroscopy of current-induced spin-orbit torques and spin accumulation in Pt/3d-transition-metal bilayers," Phys. Rev. B **100**(2), 024426 (2019).
[37]S. Ikeda, K. Miura, H. Yamamoto *et al.*, "A perpendicular-anisotropy CoFeB–MgO magnetic tunnel junction," Nat. Mater. **9**(9), 721–724 (2010).
[38]Y.-H. Wang, W.-C. Chen, S.-Y. Yang *et al.*, "Interfacial and annealing effects on magnetic properties of CoFeB thin films," J. Appl. Phys. **99**(8), 08M307 (2006).
[39]Y. Fan, H. Li, M. Dc *et al.*, "Spin pumping and large field-like torque at room temperature in sputtered amorphous WTe_{2-x} films," APL Mater. **8**(4), 041102 (2020).
[40]K. Hasegawa, Y. Hibino, M. Suzuki *et al.*, "Enhancement of spin-orbit torque by inserting CoO_x layer into Co/Pt interface," Phys. Rev. B **98**(2), 020405 (2018).
[41]S. Li, X. Zhao, W. Liu *et al.*, "Modulation of spin-orbit torque induced magnetization switching in Pt/CoFe through oxide interlayers," Appl. Phys. Lett. **114**(21), 212404 (2019).
[42]Y. Yan, C. Wan, X. Zhou *et al.*, "Strong electrical manipulation of spin–orbit torque in ferromagnetic heterostructures," Adv. Electron. Mater. **2**(10), 1600219 (2016).